Ti-B-C nanocomposite coatings deposited by magnetron sputtering

Jonas Lauridsen, N Nedfors, U Jansson, Jens Jensen, Per Eklund and Lars Hultman

Linköping University Post Print

N.B.: When citing this work, cite the original article.

Original Publication:

Jonas Lauridsen, N Nedfors, U Jansson, Jens Jensen, Per Eklund and Lars Hultman, Ti-B-C nanocomposite coatings deposited by magnetron sputtering, 2012, Applied Surface Science, (258), 24, 9907-9912.
http://dx.doi.org/10.1016/j.apsusc.2012.06.049
Copyright: Elsevier
http://www.elsevier.com/

Postprint available at: Linköping University Electronic Press
http://urn.kb.se/resolve?urn=urn:nbn:se:liu:diva-81812

Accepted Manuscript

Title: Ti-B-C nanocomposite coatings deposited by magnetron sputtering

Authors: J. Lauridsen, N. Nedfors, U. Jansson, J. Jensen, P. Eklund, L. Hultman

PII: S0169-4332(12)01099-9
DOI: doi:10.1016/j.apsusc.2012.06.049
Reference: APSUSC 23842

To appear in: *APSUSC*

Received date: 31-1-2012
Revised date: 12-6-2012
Accepted date: 14-6-2012

Please cite this article as: J. Lauridsen, N. Nedfors, U. Jansson, J. Jensen, P. Eklund, L. Hultman, Ti-B-C nanocomposite coatings deposited by magnetron sputtering, *Applied Surface Science* (2010), doi:10.1016/j.apsusc.2012.06.049

This is a PDF file of an unedited manuscript that has been accepted for publication. As a service to our customers we are providing this early version of the manuscript. The manuscript will undergo copyediting, typesetting, and review of the resulting proof before it is published in its final form. Please note that during the production process errors may be discovered which could affect the content, and all legal disclaimers that apply to the journal pertain.

ACCEPTED MANUSCRIPT

Research Highlights

- Nc-TiC:B/a-BC_x/a-C nanocomposite coatings deposited by magnetron sputtering.
- B is in a solid solution with TiC.
- B induces a rhombohedral distortion of the TiC lattice.
- A contact resistance that is comparable to Ag at loads of ~1N.

Accepted Manuscript

*Manuscript
ACCEPTED MANUSCRIPT

Ti-B-C nanocomposite coatings deposited by magnetron sputtering

J. Lauridsen[a*†], N. Nedfors[b], U. Jansson[b], J. Jensen[a], P. Eklund[a], and L. Hultman[a]

[a] *Thin Film Physics Division, Department of Physics, Chemistry, and Biology (IFM), Linköping University, SE-581 83 Linköping, Sweden*

[b] *Department of Materials Chemistry, The Ångström Laboratory, Uppsala University, P.O. Box 538, SE-751 21 Uppsala, Sweden*

Abstract

Ti-B-C nanocomposite coatings with a B content of 8-17 at. %, have been deposited by magnetron sputtering from B_4C, Ti, and C targets. X-ray diffraction, photoelectron spectroscopy, and electron microscopy show that the coatings consist of nanocrystalline (nc) TiC:B embedded in a matrix of amorphous (a) C, BC_x,TiO_x and BO_x. The fraction of amorphous phase scales with the Ti concentration, where the matrix predominantly consists of free C with some BC_x in coatings with a C/Ti ratio >1, while the matrix predominantly consists of BC_x with some free C in coatings with a C/Ti ratio <1. Nc-TiC:B/a-BC_x/a-C coatings with low amount of free C exhibit a contact resistance comparable to the contact resistance of an Ag sputtered coating at loads of ~1 N against an Au probe, despite the O content of ~16 at. %.

* Corresponding author. *E-mail address:* jonla@ifm.liu.se (J. Lauridsen).
Linköping University, IFM, SE-581 83 Linköping, Sweden. *Tel.*: +46 13282976; *Fax:* +46 13137568.
† Present adress: Seco Tools AB, SE-73782 Fagersta, Sweden.

ACCEPTED MANUSCRIPT

Keywords: Nanocrystalline; Electron microscopy; Contact resistance; B_4C; TiC

1. Introduction

Ti-B-C-based composite coatings have been studied for tribological applications [1,2,3,4], in which B increases the hardness and the wear resistance of TiC. The Ti-B-C ternary phase diagram contains TiC, TiB_2, and C. Thus, the selection of composition in the composite can give a trade-off between the lubricating amorphous C and probable BC_x phase [5] for good mechanical properties [1,2,3,4] and the hard, but also the conductive TiC/TiB_2 phases [6,7,8], for good electrical properties. Earlier work on Ti-B-C sputtered coatings has suggested that B can be incorporated into TiC [6] or that nc-TiC is embedded in a quasi-amorphous TiB_2 phase [1,2] at low B content. For high B contents, C may be incorporated into TiB_2 [6,9,10] or nc-TiB_2 may be embedded in a quasi-amorphous TiC phase [1,2]. Similar to the Ti-B-N system [11] an equiaxed nanocrystalline structure can be expected for Ti-B-C coatings due to a segregation-driven renucleation process, and that the coatings contain TiC (TiN) and TiB_2 as the thermodynamically favorable phases. The excess B would segregate to the grain surface and quench crystal growth. The above structure/property-design possibilities in the Ti-B-C system make its coatings interesting for electrical contact applications.

Today, noble metals are the most commonly used materials in electrical contacts since they have low resistivity and contact resistance, combined with chemical stability [12,13]. The high prices and the low wear resistance in some environments motivate investigations of new electrical contact materials with good electrical properties, but with better mechanical properties than the noble metals. TiC-based nanocomposite materials,

ACCEPTED MANUSCRIPT

with hard nanocrystalline (nc) TiC embedded in a softer amorphous (a) matrix, e.g., a-C or a-SiC, have been studied for electrical contact applications [14,15,16,17].

In the present study low B content Ti-B-C coatings were deposited to study the correlation of the structure and the electrical properties. The as-deposited Ti-B-C coatings are found to have lower contact resistance compared with Ti-Si-C- coatings; however, the resistivity is increased. In particular C-rich coatings are interesting to retain both lubricious and conductive phases. This together with that B improves the mechanical properties of TiC, makes the Ti-B-C system interesting as an electrical contact material.

2. Experimental details

Ti-B-C coatings were deposited by balanced dc magnetron sputtering in an ultra high vacuum deposition system [18,19] (base pressure below 6.5 x 10^{-7} Pa) from two conductive elemental targets (a 50 mm Ø Ti and a 75 mm Ø C) and one conductive compound target (a 75 mm Ø B_4C), in an Ar discharge. The targets were positioned 18 cm from the substrates, two of them at an angle of 35°, and the Ti facing them. Substrates of Si and SiO_2 wafers (both 15x15x0.5 mm), steel (15x15x1 mm), and Ni-plated Cu-6wt.% Sn (15x15x1 mm) were put on a rotating substrate holder facing the targets. During deposition, a constant dc bias of -50 V, a Ar pressure of 0.53 Pa (4 mTorr), and a substrate temperature of 300 °C were applied. Six coatings were deposited with two different B concentrations and three different C/Ti compositional ratios, respectively, under constant-current conditions, see Table 1. The sample notation is made by normalizing the Ti, B, and C contents.

ACCEPTED MANUSCRIPT

X-ray diffraction (XRD) in gracing incidence (GI) mode with an incidence angle of 2° was performed in a SIEMENS D5000 diffractometer using parallel beam geometry and a Cu Kα x-ray source operating at 45 kV and 40 mA. Stress measurements using the $\sin^2\psi$-method were performed in a PANalytical Empyrean using Cu Kα x-ray source operating at 45 kV and 40 mA.

Scanning electron microscopy (SEM) was performed in a LEO 1550 microscope. Cross-sectional images were acquired by using accelerating voltage of 10 kV with an Inlens detector. Thickness measurements were done on coatings deposited onto Si substrates.

Transmission electron microscopy (TEM) and scanning TEM (STEM) images were obtained with a Tecnai G^2 20 U-Twin 200 kV FEGTEM. Analytical TEM was made using energy-dispersive x-ray spectroscopy (EDX) in STEM mode. Cross-section samples were mechanically polished to a thickness of ~40 µm, and ion milled to electron transparency by a Gatan Precision Ion Polishing System (PIPS).

X-ray photoelectron spectroscopy (XPS) measurements were carried out using monochromatic Al Kα radiation in a Physical Electronics Quantum 2000 spectrometer. Energy calibration was carried out with Au and Ag reference samples. High resolution XPS spectra were acquired after 15 min of sputter etching with 200 eV Ar^+ ions over an area of 1x1 mm^2. The XPS analysis area was set to a diameter of 200 µm in all measurements.

Time-of-flight energy elastic recoil detection analysis (ToF-E ERDA) at the Uppsala Tandem Laboratory was employed to measure the elemental composition of the six coatings using 40 MeV $^{127}I^{9+}$ projectile ions at 22.5º incident angle and a detector placed at a recoil scattering angle of 45º [20]. The composition results were evaluated with the CONTES code [21].

ACCEPTED MANUSCRIPT

Room-temperature four-point-probe measurements were performed using a Jandel Engineering instrument with a WC probe. To obtain the resistivity, the measured sheet resistance was multiplied with the coating thickness obtained in the SEM. Contact resistance was measured with a four-wire in-house setup described in [22]. A current of 1 mA is applied and the voltage drop is measured. The contact resistance is measured both when the sample is loaded and unloaded by the Au probe. For comparison, the contact resistance is also measured on a dc magnetron sputtered Ag reference sample.

The hardness was determined by nanoindentation with an Umis 2000 instrument equipped with a Berkovich indenter. The load was 1 mN and the hardness was an average calculated according to the Oliver-Pharr method [23] from 49 indents.

A ball-on-disc test was used to measure the friction coefficient. Ball bearing steel balls, 9 mm in diameter were used against coatings deposited on steel substrates in ambient air (40 % humidity, 22 °C). The friction coefficient was continuously recorded under 5000 revolutions, with an applied load of 1 N, a sliding speed of 0.1 m/s, and a radius of the wear track of 2.5 mm. The friction coefficient value in Table 1 is an average of 5000 revolutions.

3. Results

Table 1 shows the composition of all coatings. Three coatings have a B content of ~8 at.% and three coatings have a B content of ~16 at.%, with a C/Ti ratio of ~2.7, ~1.8, and 0.8, respectively. All coatings have a O concentration of ~16 at.%. The O contamination comes most probably from the B_4C target, this is further discussed in the discussion part below.

ACCEPTED MANUSCRIPT

Figure 1 shows diffraction patterns of the coatings. The $Ti_{25}B_{10}C_{65}$ has small broad TiC peaks, with a slight peak shift to lower 2θ values. Coatings $Ti_{33}B_{10}C_{57}$ and $Ti_{49}B_{10}C_{40}$ show thinner and more intense TiC peaks, with peak shifts similar to the $Ti_{25}B_{10}C_{65}$ coating. The $Ti_{21}B_{19}C_{60}$ coating with the lowest Ti content appears XRD-amorphous, however, TEM results (below) show that all samples contain nanocrystallites of TiC. The $Ti_{27}B_{20}C_{52}$ coating exhibits small broad TiC peaks where the TiC 111 peak is shifted to lower 2θ values, while TiC 200 and 220 are not shifted. The $Ti_{43}B_{19}C_{38}$ coating has broad TiC peaks; TiC 111 is shifted to lower 2θ values, while TiC 200 and 220 are shifted to higher 2θ values. The crystallinity of the coatings increases with increased Ti content. With increased B content the peaks become broader, the intensity decreases, and the corresponding peak shifts increases. The TiC grain size is estimated by Scherrer's formula to be in the range of 2-9 nm, where coatings with larger B content have TiC grains with smaller size.

To investigate if the peak shifts in XRD are caused by stress or not, stress measurements by the $\sin^2\psi$-method on the $Ti_{43}B_{19}C_{38}$ coating were made (not shown). The $Ti_{43}B_{19}C_{38}$ coating has a compressive stress below 1 GPa, which excludes peak shifts caused by stress.

Figure 2 shows the XPS spectra in three regions from the coatings. Figure 2a shows the Ti2p region, where peaks from both $Ti2p_{3/2}$ and $Ti2p_{1/2}$ are observed at 455.0 eV, 459.1 eV, 461.0 eV, and 464.6 eV, corresponding to Ti-C and Ti-O bonds [24,25]. Note that with increased Ti content the fraction of Ti-O bonds decreases, and the peak at 455.0 eV shifts to lower bonding energies, probably corresponding to Ti-B since B has lower electronegativity than C. Figure 2b shows the C1s region, where two clear peaks are

ACCEPTED MANUSCRIPT

observed at 282.0 and 284.5 eV, attributed to C-Ti and C-C bonds, respectively [14]. In addition, there is intensity between these two peaks. It can be due to C-B bonds [26], which are expected if B is dissolved into TiC. However, it can also be due to an interfacial contribution, C-Ti*, of C at a matrix/TiC interface described by Lewin et al. [27,28,29]. It is difficult to clearly separate and fit the additional intensity in the C1s peak to these two features, but one example is shown in the top spectrum in Figure 2b, where the additional intensity appears to be mainly from C-B bonds. The $Ti_{25}B_{10}C_{65}$ and $Ti_{21}B_{19}C_{60}$ coatings with a C/Ti ratio of ~2.7, contains mainly free C, with small contributions of C-Ti and C-B. The $Ti_{33}B_{10}C_{57}$ and $Ti_{27}B_{20}C_{52}$ coatings with a C/Ti ratio of ~1.7, contains ~50:50 free C and C-Ti bonds with a small contribution from C-B, and the $Ti_{49}B_{10}C_{40}$ and $Ti_{43}B_{19}C_{38}$ coatings with a C/Ti ratio of 0.8, contains mainly C-Ti, with a low amount of C-B and free C. This means that there is a transition from manly C-C to C-Ti bonds with increased Ti content in the coatings. Figure 2c shows the B1s region, where it is observed that the coatings contain B-Ti, B-C, and B-O bonds, which originate from peaks at 188.4 eV, 189.0 eV, and 192.0 eV, respectively [26,30]. For the coatings with ~8 at.% B, a peak shift from B-C to B-Ti bonds is observed with increased Ti content in the coatings, and for the coatings with ~16 at.%, B bonds mainly to Ti.

Figure 3a shows a TEM image with corresponding SAED pattern and a HRTEM image of the $Ti_{49}B_{10}C_{40}$ coating. Columnar growth with grains of similar size is observed in the overview image. The SAED pattern shows that TiC is the only crystalline phase, consistent with the XRD results. In the HRTEM image, TiC grains with a size of ~5 nm (consistent with estimations from XRD with Scherrer's formula) in diameter are observed. Figure 3b shows a TEM image with corresponding SAED pattern and a HRTEM image

ACCEPTED MANUSCRIPT

of the $Ti_{43}B_{19}C_{38}$ coating. The coating exhibits columnar growth with slightly thinner columns than in the $Ti_{49}B_{10}C_{40}$ coating. The SAED pattern shows that the only crystalline phase is TiC, as in Coating 3. In the HRTEM image, TiC grains with a size of ~ 4 nm (consistent with estimations from XRD) are observed. Figure 3c shows the corresponding information from the $Ti_{21}B_{19}C_{60}$ coating. The overview TEM image shows a featureless structure, without the columnar morphology found in the $Ti_{49}B_{10}C_{40}$ and $Ti_{43}B_{19}C_{38}$ coatings. The SAED pattern shows blurry rings, indicating nanocrystalline TiC. ~3 nm (consistent with estimations from XRD) large TiC grains are observed in the HRTEM image.

Figure 4 shows the contact resistance of all coatings and an Ag reference. The $Ti_{25}B_{10}C_{65}$ and $Ti_{21}B_{19}C_{60}$ coatings, with the C/Ti ratio of 2, have the highest contact resistance (~20 mΩ at 1N). The other coatings have a contact resistance of ~7 mΩ at loads of ~1 N, which is ~5 times higher than the sputtered Ag reference.

Table 1 shows the resistivity of all coatings. The resistivity of the coatings (thickness 370-690 nm) is in the range 380-3990 μΩ cm depending on the C/Ti ratio. Decreased C/Ti ratio decreases the resistivity.

The hardness of the coatings is in the range of 10-16 GPa (see Table 1). Increased Ti content increases the hardness of the coating; increased B content has no significant effect on the hardness.

ACCEPTED MANUSCRIPT

Table 1 also shows the friction coefficient of four coatings. The friction coefficient was in the range 0.19-0.33. Unfortunately, the substrates where coatings $Ti_{21}B_{19}C_{60}$ and $Ti_{27}B_{20}C_{52}$ were deposited were too rough for the ball-on-disc measurements to give meaningful results for these two samples.

4. Discussion

4.1 Distribution of B

An important question is: how is B distributed in the coating? The results indicate that B is in solid solution on C sites in the TiC lattice as presented as a possibility by ref [6,9], and is part of an amorphous B-C matrix, but does not form TiB_2 [1,2]. The peak shift in XRD with increased B content would correspondingly be due to the incorporation of B into TiC. If all Ti in the coating is in the TiC phase, the amount of B that is incorporated into the TiC:B can be estimated from XPS data. Thus, the XRD peak shift scales with the amount of B incorporated into TiC:B. For our Ti-B-C coatings, the TiC 111 is shifted to lower 2θ, i.e., a larger cell parameter, in agreement with the larger atom radii of B compared with C. However, for the $Ti_{43}B_{19}C_{38}$ coating, the TiC 200 and 220 peaks are shifted to larger 2θ values. This indicates that B is preferentially located at the {111} planes, which also can occur in bulk TiC:B [31]. As the cubic symmetry is interrupted, it yields a rhombohedral TiC:B structure. The rhombohedral distortion of the cubic unit cell in the present coatings is connected with elongation of the body diagonal [111] and a contraction in the other diagonals. This explains why the TiC 111 peak is shifted to lower 2θ values and TiC 200 and 220 is shifted to higher 2θ values [32]. The possibility that the peak shift in XRD could be due to that the coatings contain both nanocrystalline TiC and TiB_2, which has been suggested earlier in both Ti-B-C and Ti-C-

ACCEPTED MANUSCRIPT

N coatings, [1,2,11] is excluded on the following grounds: in [1,2] a shift in XRD from nc-TiC and quasi-amorphous TiB_2, to nc-TiB_2 and quasi-amorphous TiC with increased B content is observed. In [1] it is also shown with SAED that TiB_2 is formed at a B/Ti ratio of 1.2, while TiC is formed at a B/Ti ratio of 0.4, indicating that the formation of TiB_2 requires a high B concentration. In the coatings studied here, the B content is only 8-16 at.%, favoring the formation of nc-TiC. This is supported by our HRTEM and SAED analyses, which show only crystalline TiC phase grains and no TiB_2. The broad rings in SAED are obviously a consequence of the small grain size. Although the HRTEM images of the $Ti_{43}B_{19}C_{38}$ coating shows lattice fringes with d-values of ~2.62 nm, which fits TiB_2 (100), no other set of planes could be seen from that phase. Instead, this large d-spacing can be explained as the result of incorporation of B into TiC. Similarly, no TiB_2 grains were found in the HRTEM images from the $Ti_{21}B_{19}C_{60}$ and $Ti_{49}B_{10}C_{40}$ coatings. Also, the typical XTEM overview image of the coatings (see Figure 3a), shows a columnar structure, from the extended growth of TiC as has been indicative for TiC/C nanocomposite growth [15, 25]. In contrast, B-rich Ti-B-C coatings have a more homogenous if not featureless structure as TiB_2 tends to form in the coatings [1,11].

Worth mentioning is also that with increased Ti and B content, B bonds to C, and the BC_x concentration increases in the amorphous matrix since the concentration of free C decreases. This means that with increased Ti and B content the amorphous matrix that first consist mostly of free C is replaced by BC_x.

ACCEPTED MANUSCRIPT

4.2 Composition of the amorphous matrix

The higher intensity of the XRD TiC:B peaks from the $Ti_{33}B_{10}C_{57}$ and $Ti_{27}B_{20}C_{52}$ coatings compared with the $Ti_{25}B_{10}C_{65}$ and $Ti_{21}B_{19}C_{60}$ coatings indicate that increased Ti content lead to higher crystallinity of the coatings. However, the coatings with higher B content have lower crystallinity, indicating that the B impedes TiC growth, which is in agreement with [1,2]. This is also supported from the overview TEM images, where it is observed that the $Ti_{43}B_{19}C_{38}$ coating with higher B content than the $Ti_{49}B_{10}C_{40}$ coating has a smaller column width.

The matrix in the $Ti_{25}B_{10}C_{65}$ and $Ti_{21}B_{19}C_{60}$ coatings consists mainly of free C. In agreement with previous reports [22], an increased amount of amorphous matrix correlates with a decreased grain size in TiC-based nanocomposites. Therefore, in $Ti_{21}B_{19}C_{60}$ the growth of crystalline phases is quenched. It is interesting that essentially crystalline coatings can be obtained by adding only a few atomic percent Ti. This was the case for the $Ti_{25}B_{10}C_{65}$ coating. Higher Ti content also results in decreased amount of free C, and higher concentration of TiC:B, which leads to lower amount of amorphous matrix that can quench the grain growth. The $Ti_{49}B_{10}C_{40}$ and $Ti_{43}B_{19}C_{38}$ coatings with the highest Ti content have the highest peak intensity in XRD, indicating the highest crystallinity of the coatings. These coatings contain no or just a small amount of free C; all C is instead bonded to Ti or B. In the Ti2p region from the XPS spectra, the peak at 455 eV is shifted to lower binding energies, meaning that a higher concentration of Ti bonds to B instead of C. The peak shift in Ti2p with increased Ti content is supported by a peak shift in the B1s region, from B-C bonds to more B-Ti bonds. With an increased Ti content more B is incorporated into the TiC:B, and the amorphous matrix that has mostly contained free C and BC_x will now mostly consist of BC_x.

ACCEPTED MANUSCRIPT

The O (~16 at. % O) contamination comes most probably from the B_4C target since an O content of 8 at.% through the target was determined with XPS. Similar values of O in other Ti-B-C coatings have been reported in the literature, where the explanation has been additional O absorption by Ti in the TiC:TiB_2 target [10,33]. However, the O content were higher in coatings with higher B content [10], indicating that it is the B that absorbs O. That is what we think happens in our coatings, i.e., B in the B_4C target absorb O. The matrix is affected by the O content in that way that O is bonded to both Ti and B. From XPS data it is seen that the Ti-O contribution decreases with increased Ti content, and that the B-O contribution increases with increased B content, probably since Ti forms carbide instead, and that more B is available. However, it is unclear how the O is distributed, if it is only randomly in the matrix, or if it is located around the crystalline grains.

4.3 Electrical properties

The change in phase composition of the TiC:B and the amorphous matrix with increased Ti content, also decreases the resistivity as well as the contact resistance of the coatings. The $Ti_{25}B_{10}C_{65}$ and $Ti_{21}B_{19}C_{60}$ coatings with high amount of free C have the highest resistivity and contact resistance. The $Ti_{43}B_{19}C_{38}$ coating with the highest amount of Ti and B has the lowest resistivity and contact resistance, a contact resistance comparable with Ti-A-C-Ag (A = Si, Ge, Sn or Cu) nanocomposite coatings [34] and Ag against an Au probe at loads of ~1 N. This is because a higher Ti content leads to higher concentration of the crystalline phase, the phase that is the most conductive in this material system. Increased B content for the corresponding coatings leads to higher

ACCEPTED MANUSCRIPT

incorporation of B into the TiC:B, and lower resistivity and contact resistance, indicating that TiC:B is more conductive than TiC.

Both TiB_2 (270 μΩ cm) and TiC (80 μΩ cm) coatings have lower resistivity than the Ti-B-C coatings [35,36], however, these coatings are too hard and brittle which leads to increased contact resistance [15]. The resistivity for the Ti-B-C coatings are in general also higher (~10^3 μΩ cm) than for Ti-A-C-Ag (A = Si, Ge, Sn or Cu) coatings (~10^2 μΩ cm) [22] or for other comparable nanocomposites [37,38,39,40]. However, the contact resistance is comparable, and the contact resistance is just a factor ~5 larger than for Ag against Ag, which is remarkable since the coatings contains ~16 at.% O. It is unclear how much the O affects the electrical properties, but the O contamination is expected to increase both the resistivity and the contact resistance significantly. Nevertheless, these O containing Ti-B-C coatings have qualities as electrical contact material.

4.4 Mechanical properties

The hardness of the coatings is lower than for TiC [25], and also lower than in earlier reports on the hardness of Ti-B-C coatings [41,42], and it did not increase with the incorporation of B, which was reported before [1,2,3,4]. This is probably an affect off a larger fraction of soft amorphous matrix in these coatings compared with [41,42]. This also explains the low coefficient of friction against steel, with values comparable to what was published in [41]. The friction coefficients in these Ti-B-C coatings do not seem to vary significantly, which means that the increased amount of free C did not improve the tribological behavior. How large affect the incorporation of O into the coatings has on the mechanical properties is unclear. That the coatings have a hardness of ~12 GPa is not a drawback in an electrical contact application, it is harder than the noble metals, and has a

ACCEPTED MANUSCRIPT

lower coefficient of friction compared with Ag against Ag (μ = 1.2) [22], which make these coatings promising as electrical contact material.

5. Conclusions

Ti-B-C nanocomposite coatings with low B content deposited by magnetron sputtering from B_4C, Ti, and C targets consist of nanocrystalline (nc) TiC:B embedded in a matrix of amorphous (a) C, BC_x, TiO_x, and BO_x. The most likely position of B in the coatings is as a solid solution with TiC with a rhombohedral distortion of the cubic structure from ordering on the {111} planes. The amount of amorphous matrix in the coatings is controlled by the Ti content. Increased Ti content leads to less free C and more BC_x in the matrix, and more B incorporated into the TiC:B. In consequence, the contact resistance is lowered for the coatings against an Au probe at loads of ~1 N to values comparable to Ag, in spite of the high resistivity and a O content of ~16 at.%. Thus, nc-TiC:B/a-BC_x/a-C coatings present an interesting alternative as electrical contact material.

Acknowledgments

The authors whish to acknowledge Fang Mao at the department of Chemistry, Ångström Laboratory, Uppsala University, for the assistance with the ball-on-disk measurements. The work was financially supported by the VINNOVA VINN Excellence Centre in Research and Innovation on Functional Nanoscale Materials, *FunMat*.

ACCEPTED MANUSCRIPT

Table 1. The composition determined with ERDA, resistivity, hardness, and friction coefficient of the coatings.

Coating	C [at.%]	Ti [at.%]	B [at.%]	O [at.%]	C/Ti	Resistivity (μΩ cm)	Hardness (GPa)	μ_{Steel}
1($Ti_{25}B_{10}C_{65}$)	55	21	8	16	2.6	2590	10	0.29
2($Ti_{33}B_{10}C_{57}$)	47	27	8	17	1.7	1840	12	0.19
3($Ti_{49}B_{10}C_{40}$)	35	43	9	13	0.8	850	16	0.33
4($Ti_{21}B_{19}C_{60}$)	50	18	16	16	2.8	3990	10	-
5($Ti_{27}B_{20}C_{52}$)	44	23	17	16	1.9	1100	11	-
6($Ti_{43}B_{19}C_{38}$)	32	36	16	16	0.9	380	16	0.31

Accepted Manuscript

ACCEPTED MANUSCRIPT

Figure 1. GI-XRD diffractograms of all coatings.

Figure 2. XPS spectra from three regions, a) Ti2p, b) C1s, and c) B1s, of all coatings.

Figure 3. TEM overview micrograph with corresponding SAED pattern and HRTEM image from a) $Ti_{49}B_{10}C_{40}$, b) $Ti_{43}B_{19}C_{38}$, and c) $Ti_{21}B_{19}C_{60}$ coatings. Some of the nanocrystalline grains are outlined by solid lines.

Figure 4. Contact resistance measurements of all coatings and a sputter deposited Ag reference.

Accepted Manuscript

ACCEPTED MANUSCRIPT

[1] C. Mitterer, P. H. Mayrhofer, M. Beschliesser, P. Losbichler, P. Warbichler, F. Hofer, P. N. Gibson, W. Gissler, H. Hruby, J. Musil, J. Vlček, Surf. Coat. Technol. 120-121 (1999) 405-411.

[2] J.-T. Ok, I.-W. Park, J. J. Moore, M. C. Kang, K. H. Kim, Surf. Coat. Technol. 200 (2005) 1418-1423.

[3] D. Vallauri, I. C. Atias Adrián, A. Chrysanthou, J. Eur. Ceram. Soc. 28 (2008) 1697-1713.

[4] M. Stüber, V. Schier, H. Holleck, Surf. Coat. Technol. 74-75 (1995) 833-837.

[5] S. Yoon, J. Kim, B. D. Kim, C. Lee, Surf. Coat. Technol. 205 (2010) 1962-1968.

[6] C. Mitterer, M. Rauter, P. Rödhammer, Surf. Coat. Technol., 41 (1990) 351-363.

[7] G. B. Raju, B. Basu, A. K. Suri, Int. J. Refract. Met. Hard Mater. 28 (2010) 174-179.

[8] C. M. T. Sanchez, B. Rebollo Plata, M. E. H. Maia da Costa, F. L. Freire Jr. Surf. Coat. Technol. 205 (2011) 3698-3702.

[9] O. Knotek, R. Breidenbach, F. Jungblut, F. Löffler, Surf. Coat. Technol., 43 (1990) 107-115.

[10] M. D. Abad, J. C. Sánchez-López, M. Brizuela, A. Garcia-Luis, D. V. Shtansky, Thin Solid Films 518 (2010) 5546-5552.

[11] P. H. Mayrhofer, C. Mitterer, J. G. Wen, I. Petrov, J. E. Greene, J. Appl. Phys., 100 (2006) 044301.

[12] M. Antler, Thin Solid Films 84 (1981) 245-256.

[13] P. G. Slade, ed., *Electrical Contacts – Principles and Applications*, CRC Press, Taylor & Francis Group, New York, 1999.

Accepted Manuscript

ACCEPTED MANUSCRIPT

[14] E. Lewin, O. Wilhelmsson, U. Jansson, J. Appl. Phys. 100 (2006) 054303.

[15] P. Eklund, J. Emmerlich, H. Högberg, O. Wilhelmsson, P. Isberg, J. Birch, P. O. Å. Persson, U. Jansson, L. Hultman, J. Vac. Sci. Technol. B 23 (2005) 2486-2495.

[16] J. Lauridsen, P. Eklund, J. Jensen, H. Ljungcrantz, Å. Öberg, E. Lewin, U. Jansson, A. Flink, H. Högberg, L. Hultman, Acta Materialia 58 (2010) 6592-6599.

[17] U. Jansson, E. Lewin, M. Råsander, O. Eriksson, B. André, U. Wiklund, Surf. Coat. Technol. 206 (2011) 583-590.

[18] J. Emmerlich, H. Högberg, S. Sasvári, P. O. Å. Persson, L. Hultman, J.-P. Palmquist, U. Jansson, J. M. Molina-Aldareguia, Z. Czigány, J. Appl. Phys. 96 (2004) 4817-4826.

[19] J. Frodelius, P. Eklund, M. Beckers, P.O.Å. Persson, H. Högberg, L. Hultman, Thin Solid Films 518 (2010) 1621-1626.

[20] Y. Zhang, H. J. Whitlow, T. Winzell, I. F. Bubb, T. Sajavaara, J. Jokinen, K. Arstila, J. Keinonen, Nucl. Instrum. Methods Phys. Res. B 149 (1999) 477-489.

[21] M. S. Janson, CONTES instruction manual, 2004.

[22] J. Lauridsen, TiC-based nanocomposite coatings as electrical contacts, PhD Thesis, ISBN: 978-91-7393-030-7, Linköping, Sweden, 2011.

[23] W. C. Oliver, G. M. Pharr, J. Mater. Res. 7 (1992) 1564-1580.

[24] J. Chastain, R. King Jr., Handbook of X-ray Photoelectron Spectroscopy, Physical Electronics, Eden Prarie, MN, 1995.

[25] J. Lauridsen, P. Eklund, T. Joelsson, H. Ljungcrantz, Å. Öberg, E. Lewin, U. Jansson, M. Beckers, H. Högberg, L. Hultman, Surf. Coat. Technol. 205 (2010) 299-305.

Accepted Manuscript

ACCEPTED MANUSCRIPT

[26] H. A. Castillo, E. Restrepo-Parra, J. M. Vélez, W. de la Cruz, Surf. Coat. Technol. 205 (2011) 3607-3612.

[27] E. Lewin, P. O. Å. Persson, M. Lattemann, M. Stüber, M. Gorgoi, A. Sandell, C. Ziebert, F. Schäfers, W. Braun, J. Halbritter, S. Ulrich, W. Eberhardt, L. Hultman, H. Siegbahn, S. Svensson, U. Jansson, Surf. Coat. Technol. 202 (2008) 3563-3570.

[28] E. Lewin, M. Gorgoi, F. Schäfers, S. Svensson, U. Jansson, Surf. Coat. Technol. 204 (2009) 455-462.

[29] M. Magnuson, E. Lewin, L. Hultman, U. Jansson, Phys. Rev. B 80 (2009) 235108.

[30] R. Gilmore, M. A. Baker, P. N. Gibson, W. Gissler, Surf. Coat. Technol. 105 (1998) 45-50.

[31] G. E. Hollox, Microstructure and mechanical behavior of carbides, seventh technical report, NASA, 1968.

[32] N. A. Dubrovinskaia, L. S. Dubrovinsky, S. K. Saxena, R. Ahuja, B. Johansson, J. Alloys Compd. 289 (1999) 24-27.

[33] S. Shimada, M. Takahashi, J. Tsujino, I. Yamazaki, K. Tsuda, Surf. Coat. Technol. 201 (2007) 7194-7200.

[34] J. Lauridsen, P. Eklund, J. Jensen, A. Furlan, A.Flink, A.M. Andersson, U. Jansson, L. Hultman, Thin Solid Films 520 (2012) 5128-5136.

[35] A. Shutou, T. Matsui, H. Tsuda, H. Mabuchi, K. Morii, Mat. Lett., 45 (2000) 143-148.

[36] H. Högberg, J. Birch, M. Odén, J.-O. Malm, L. Hultman, U. Jansson, J. Mater. Res. 16 (2001) 1301-1310.

[37] J. E. Krzanowski and J. L. Endrino, Mater. Lett. 58 (2004) 3437-3440.

Accepted Manuscript

ACCEPTED MANUSCRIPT

[38] M. D. Abad, J. C. Sánchez-López, N. Cusnir, R. Sanjinés, J. Appl. Phys. 105 (2009) 033510.

[39] M.D. Abad, R. Sanjinés, J.L. Endrino, R. Gago, J. Andersson, J.C. Sánchez-López Plasma Process and Polym. 8 (2011) 579-588.

[40] P. Eklund Surface Engineering 23 (2007) 406-411.

[41] M. D. Abad, D. Cáceres, Y. S. Pogozhev, D. V. Shtansky, J. C. Sánchez-López, Plasma Process. Polym. 6 (2009) S107-S112.

[42] M. Y. Liu, J. Y. Yan, S. Zhang, L. Dong, M. Cao, X. Y. Deng, D. J. Li, IEEE Transactions on Plasma Science 39 (2011) 3115-3119.

Accepted Manuscript

Figure(s)

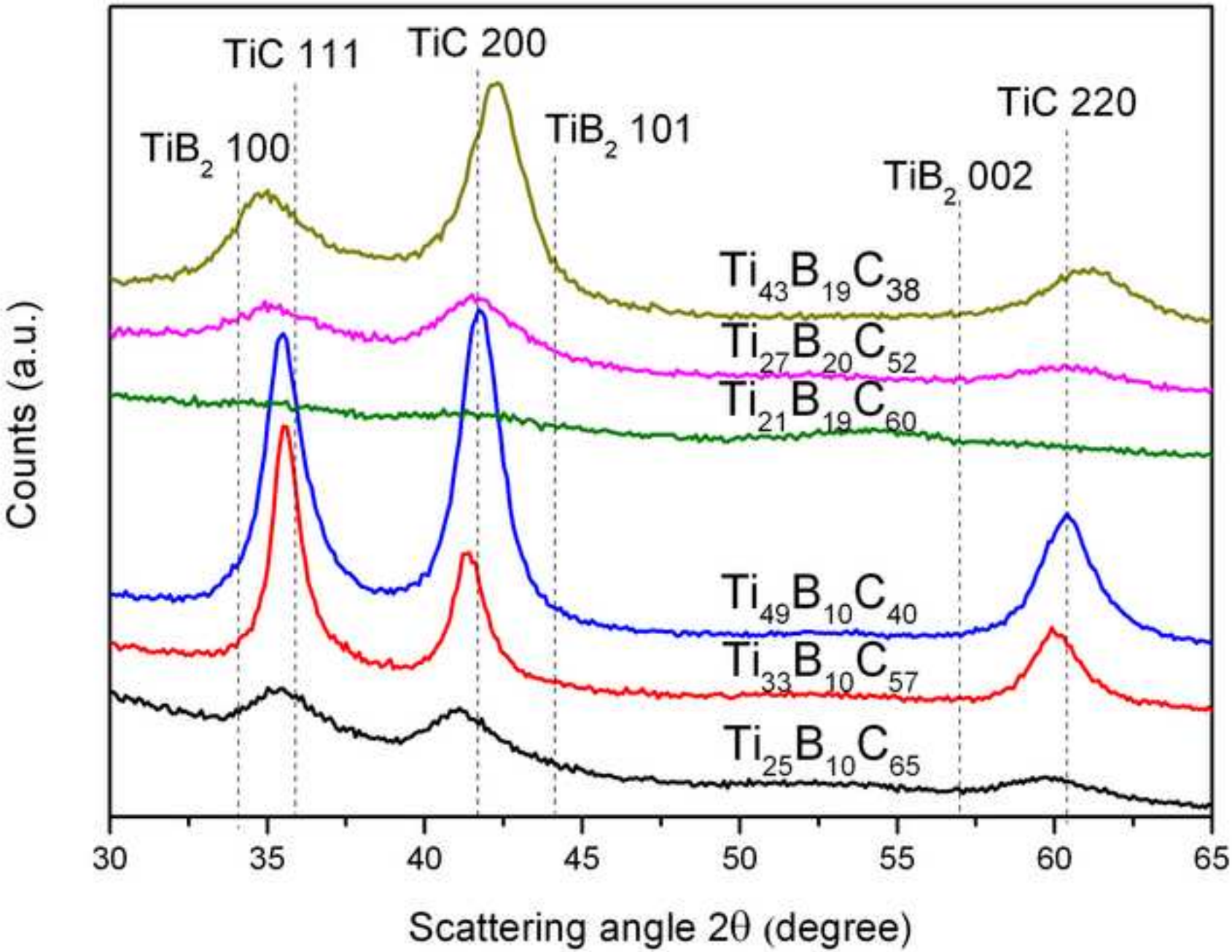
TiC 111
TiC 200
TiC 220
TiB2 100
TiB2 101
TiB2 002
Ti43B19C38
Ti27B20C52
Ti21B19C60
Ti49B10C40
Ti33B10C57
Ti25B10C65
Counts (a.u.)
30
35
40
45
50
55
60
65
Scattering angle 2θ (degree)

Figure(s)

a)

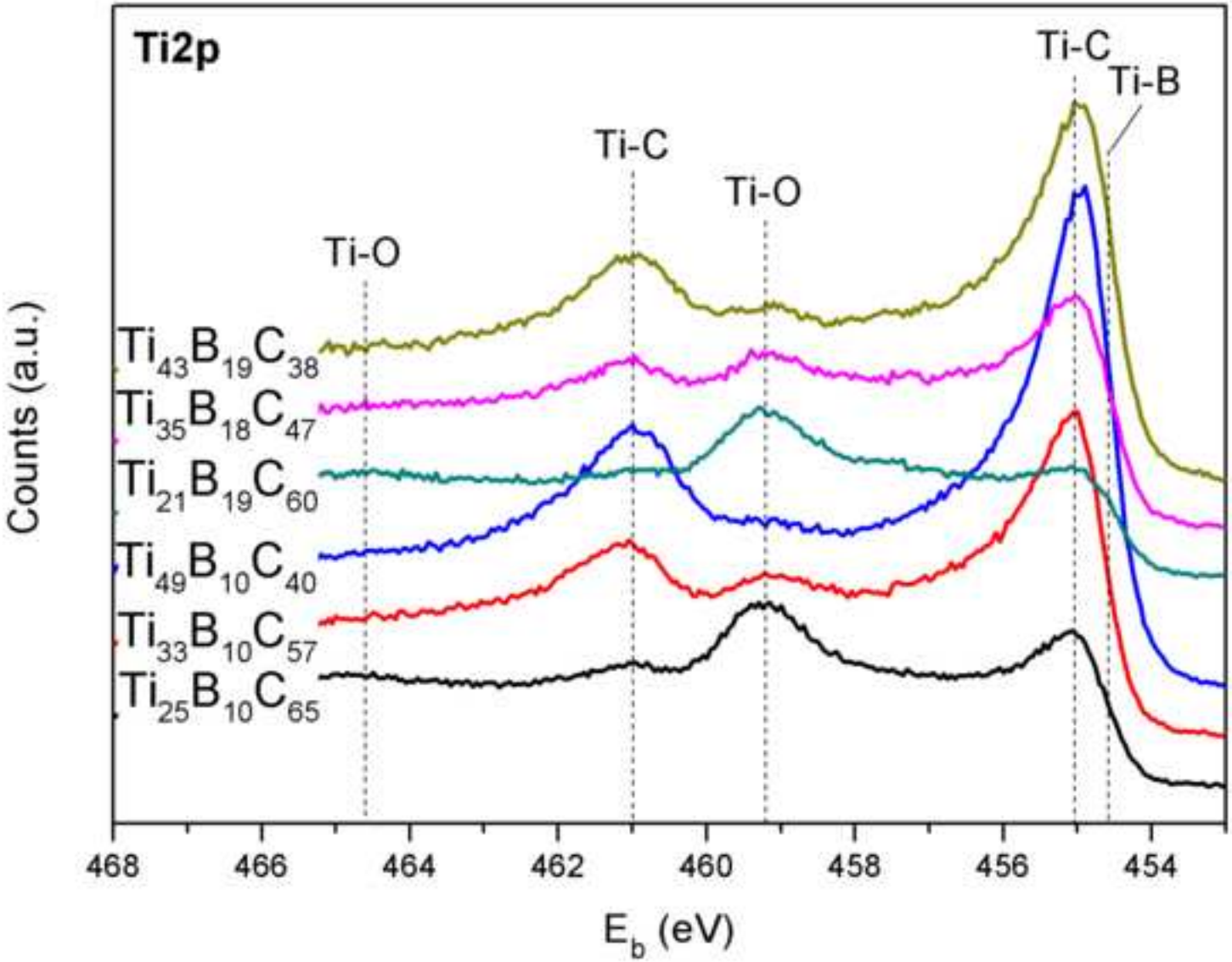
Ti2p
Ti-C
Ti-B
Ti-C
Ti-O
Ti-O
Counts (a.u.)
$Ti_{43}B_{19}C_{38}$
$Ti_{35}B_{18}C_{47}$
$Ti_{21}B_{19}C_{60}$
$Ti_{49}B_{10}C_{40}$
$Ti_{33}B_{10}C_{57}$
$Ti_{25}B_{10}C_{65}$
468
466
464
462
460
458
456
454
E_b (eV)

b)

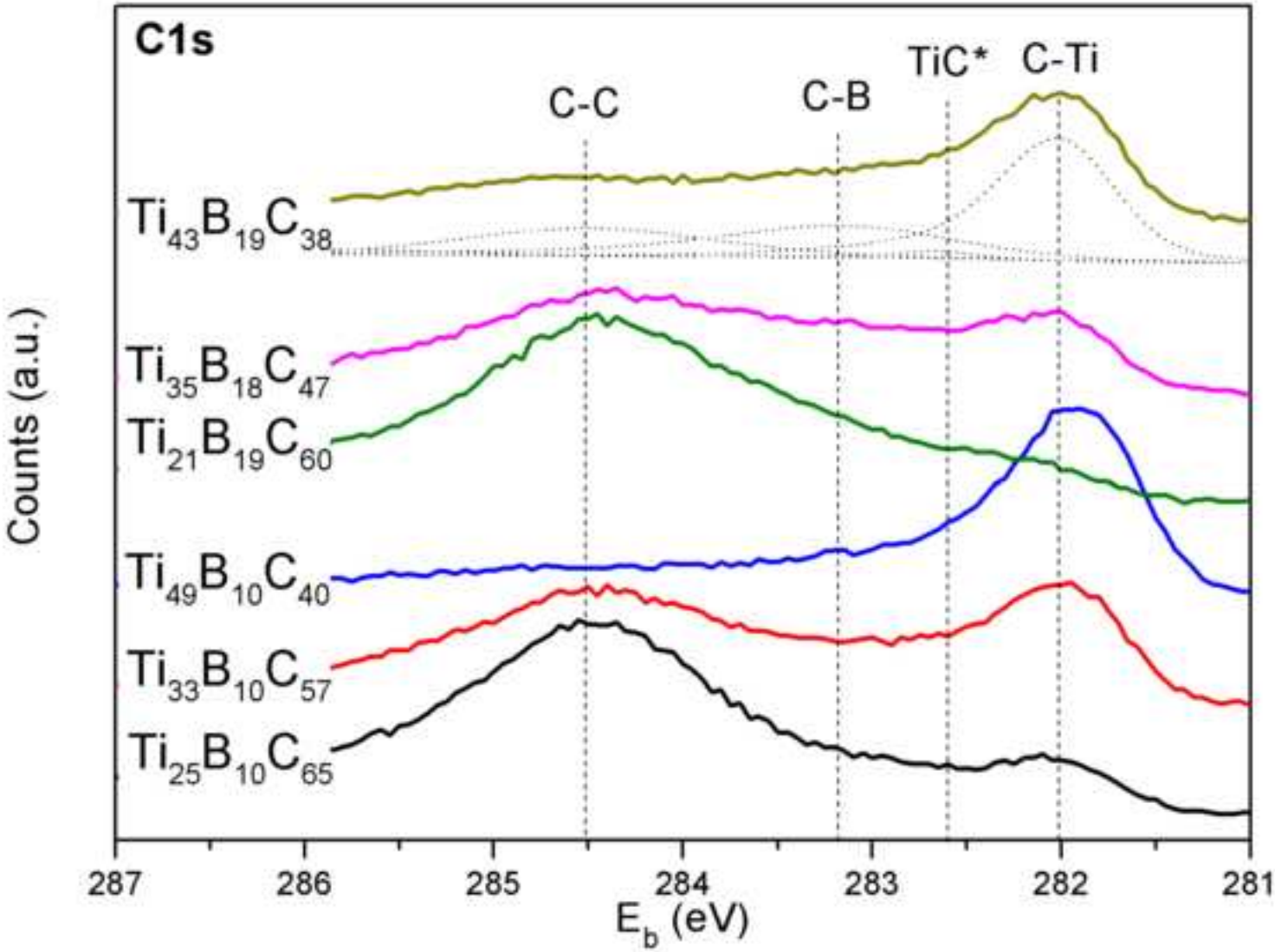
C1s
C-C
C-B
TiC*
C-Ti
Ti43B19C38
Ti35B18C47
Ti21B19C60
Ti49B10C40
Ti33B10C57
Ti25B10C65
Counts (a.u.)
287
286
285
284
283
282
281
Eb (eV)

c)

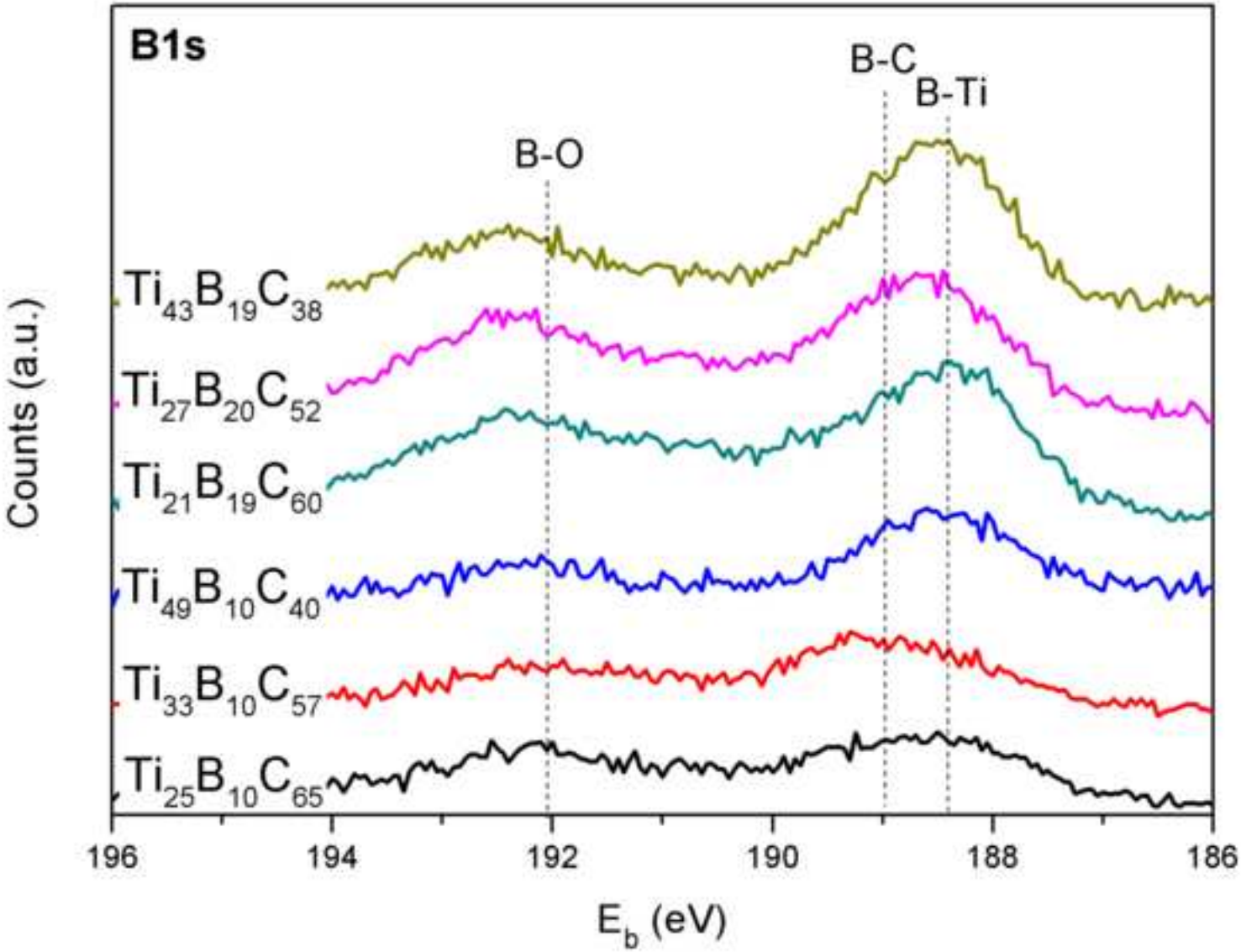
B1s
B-C
B-Ti
B-O
Ti43B19C38
Ti27B20C52
Ti21B19C60
Ti49B10C40
Ti33B10C57
Ti25B10C65
Counts (a.u.)
196
194
192
190
188
186
Eb (eV)

ACCEPTED MANUSCRIPT

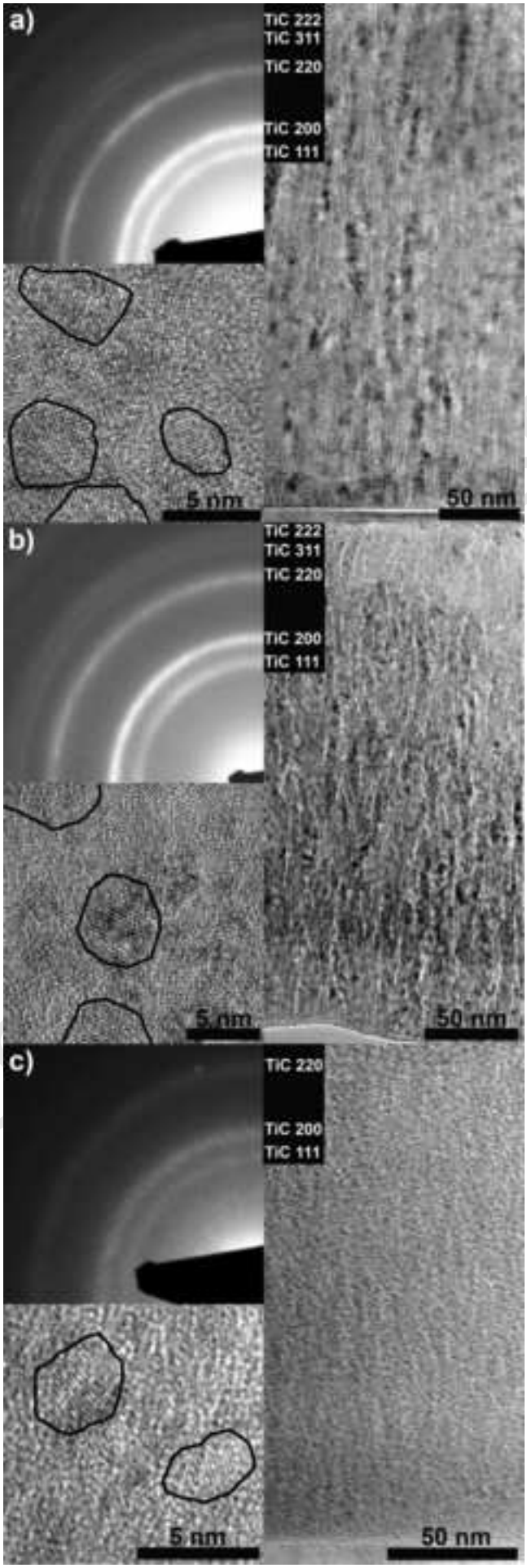

Accepted Manuscript

Figure(s)

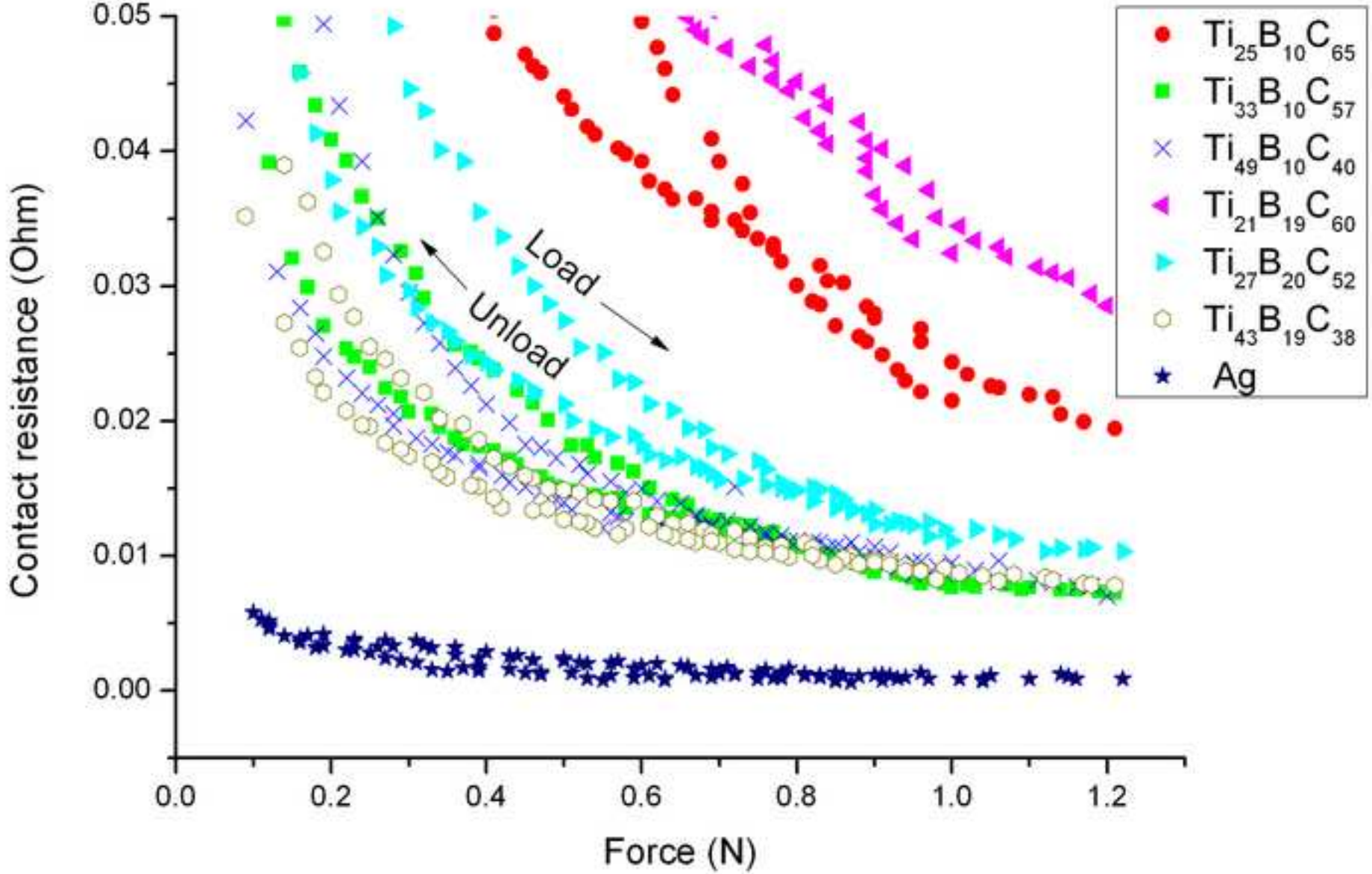
Contact resistance (Ohm)
Force (N)
0.05
0.04
0.03
0.02
0.01
0.00
0.0
0.2
0.4
0.6
0.8
1.0
1.2
Load
Unload
$Ti_{25}B_{10}C_{65}$
$Ti_{33}B_{10}C_{57}$
$Ti_{49}B_{10}C_{40}$
$Ti_{21}B_{19}C_{60}$
$Ti_{27}B_{20}C_{52}$
$Ti_{43}B_{19}C_{38}$
Ag